JPEDAV (2009) 30:309–317
DOI: 10.1007/s11669-009-9556-4
1547-7037 ©ASM International

Phase Characteristics of a U-22Pu-4Am-2Np-40Zr Metallic Alloy Containing Rare Earths

Douglas E. Burkes, J. Rory Kennedy, Thomas Hartmann, and Leah N. Squires

(Submitted December 17, 2008; in revised form April 23, 2009)

Metallic fuel alloys consisting of uranium (U), plutonium (Pu), and zirconium (Zr) with minor additions of americium (Am) and neptunium (Np) are under evaluation for potential use to transmute long-lived transuranic actinide isotopes in fast reactors. The current irradiation test series design, designated Advanced Fuel Cycle-2 (AFC2), includes minor additions of rare earth (RE) elements to simulate expected fission product carryover from the electrochemical molten salt reprocessing technique. The as-cast fuel alloys have been investigated for phase and thermal properties; specifically, enthalpies of transition, transition temperatures, and room temperature phase characteristics. Results and observations related to these characteristics for the "fresh" fuel alloys are provided. The alloy compositions are based on a U-22Pu-4Am-2Np-40Zr alloy, along with additions of 1.3 and 1.9 at.% RE (at the expense of uranium where RE denotes rare earth alloy of cerium, lanthanum, praseodymium, and neodymium). Phase behavior and associated transitions have been compared to available U-Pu-Zr ternary diagrams with acceptable agreement. Enthalpies of transition were deconvoluted from heating and cooling thermal traces for relatively reliable values. The RE additions to the base alloy have a minimal influence on the room temperature phases present and phase transition temperatures, but the room temperature phases present did impact the enthalpies of transition.

Keywords energy production, hydrogen production, metallic fuel alloys, minor actinides, phase identification, rare earths, spent light water reactor fuel, thermal properties analysis, water production, x-ray diffraction

1. Introduction

Spent light water reactor (LWR) fuel contains a small amount of long-lived minor actinides (MA) neptunium (Np), americium (Am), and curium (Cm). These MAs can be readily separated from the spent nuclear fuel employing pyroprocessing or aqueous processing schemes. Development of fuel alloys containing the separated MAs for use in the transmutation of long-lived fission products is one of the top goals of the Advanced Fuel Cycle (AFC) program. In doing so, the waste management scheme for spent nuclear fuel will become much simpler. It will hopefully increase public support for commercial nuclear power generation and possibly generate a respectable amount of heat for energy, hydrogen, or water production, meanwhile maintaining a proliferation resistant operational scheme.[1,2] Fuels for fast reactors must behave in a benign manner during core off-normal events, maintain integrity up to a high burnup, lend themselves to low-loss recycling processes, and must be easily fabricated with minimal material loss in a remote handling environment. Alloys of U-Pu-Zr satisfy these requirements with exceptional fuel cladding chemical interaction resistance, but with the disadvantage of creep at 750 °C, and increased shock sensitivity.

Several thousand metal fuel pins were fabricated in support of the Experimental Breeder Reactor-II (EBR-II) reactor in Idaho during the 1960s through the 1980s.[3] A number of fuel designs (designated as Mark) were explored, including alloys that consisted of U-Fs, U-Zr, and U-Pu-Zr. A minimal number of irradiations were carried out on the U-Pu-Zr fuel alloy that ultimately was to be used to convert

Douglas E. Burkes, J. Rory Kennedy, Thomas Hartmann, and **Leah N. Squires**, Nuclear Fuels and Materials Division, Idaho National Laboratory, P.O. Box 1625, Idaho Falls, ID 83415-6188, USA. Contact e-mail: Douglas.Burkes@inl.gov.

Abbreviations

AFC	Advanced Fuel Cycle
AL	INL Analytical Laboratory
Am	americium
BOL	beginning of life
Cm	curium
DSC	differential scanning calorimeter
EBR-II	Experimental Breeder Reactor—II
FMF	INL Fuel Manufacturing Facility
INL	Idaho National Laboratory
LWR	light water reactor
MA	minor actinide
Np	neptunium
Pu	plutonium
RE	rare earth
TGA	Thermogravimetric Analyzer
U	uranium
XRD	x-ray diffraction
Zr	zirconium

the driver core of EBR-II before it was terminally shut down in 1994. Thus, a limited characterization and performance database is available on these particular alloy systems. Beginning of life (BOL) phase behavior is an important characteristic to investigate the performance and behavior of the fuel alloy as a function of irradiation, i.e., operating temperature, fission rate, and burnup. For example, differences in phase behavior could result from different thermal histories of the fresh fuel alloys and those placed in-reactor, or could be caused by changes during irradiation. It is important to a fuels development campaign to separate these changes in order to affect fuel fabrication techniques to optimize microstructural characteristics and to relate behavioral differences of well-characterized fuels at BOL and post-irradiation. The alternative to such investigations is to irradiate a number of samples with poorly characterized BOL properties. Furthermore, adequate understanding of phase behavior can be a powerful tool in developing and verifying predictive modeling tools, both in terms of fabrication processes and irradiation performance.

Thus, an adequate understanding of how MA and RE element additions affect the thermal and phase behavior of nominal metallic fuel alloy compositions is of importance for continued development of fast reactor concepts. The objective of this study is to investigate these behaviors on a U-22Pu-4Am-2Np-40Zr (nominal atomic percentages) metal fuel alloy prior to irradiation, with up to 1.9 at.% RE addition.

2. Experimental Materials and Methods

Three metal alloys were investigated: a base alloy of nominal composition U-22Pu-4Am-2Np-40Zr and two alloys each with 1.3 and 1.9 at.% RE that was substituted for U. The RE itself was an alloy of nominal composition 0.32 at.% Ce, 0.08 at.% La, 0.20 at.% Pr, and 0.66 at.% Nd, representing an approximate RE carryover composition. Although not anticipated to affect the properties measured herein, the U used in these samples had a varying enrichment, as defined by Table 1. Throughout this paper, these alloys will be referred to as Alloy-D, Alloy-E, and Alloy-F as defined in Table 1. All alloy samples had less than 340 ppm Fe contaminant. Likewise, the alloy samples contained less than 1000 ppm Cu contaminant, except for Alloy-D that contained 3210 ppm Cu contaminant.

2.1 Alloy and Sample Preparation

An arc-melting process was used to melt and homogenize the metallic fuel alloys as defined in Table 1.[4] Right cylindrical fuel slugs, approximately 5 mm in diameter and 20 mm in length, were cast from the homogenized melt using yttria-coated quartz molds. The casting was removed by breaking the quartz mold, followed by sectioning the slug into multiple samples, each approximately 1 mm thick employing a low speed, diamond blade saw for characterization. Further sample preparation ensured a flat surface for maximum contact (Differential Scanning Calorimeter [DSC]) and x-ray beam exposure (x-ray diffraction [XRD]). A sample from one slug casting was used for thermal analysis, while three samples from three separate slug castings were used for phase determination. An example microstructure for Alloy-F is shown in Fig. 1. The photomicrograph reveals the presence of a multiphase mixture with a two-phase matrix consistent with previous

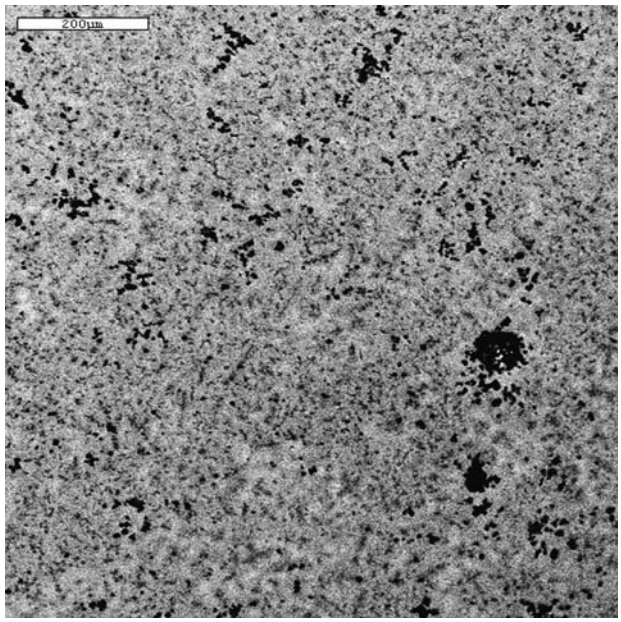

Fig. 1 Sample microstructure of Alloy-F taken in backscattered electron mode in a scanning electron microscope. Note the appearance of a two-phase matrix and Zr-rich inclusions (black, globular formations)

Table 1 Percentage of alloying metals that comprise the experimental fuels (Alloy-D, Alloy-E, and Alloy-F) for this study (nominal atomic percentages)

Alloy	U_{tot}	Pu_{tot}(a)	Am	Np	Zr	RE(b)	^{235}U, %
D	34.5 (30.6)	22.7 (22.1)	3.2 (3.7)	2.0 (2.3)	35.8 (39.4)	1.8 (1.9)	45
E	31.7 (31.1)	21.7 (22.2)	4.0 (3.7)	2.0 (2.3)	39.3 (39.5)	1.3 (1.3)	55
F	31.3 (32.0)	20.9 (22.3)	4.0 (3.7)	2.5 (2.3)	41.4 (39.7)	0.0 (0.0)	93

Actual percentages of the samples are presented with the target percentages in parentheses
(a)Pu_{tot} is composed of the isotopes 0.06% ^{238}Pu, 83% ^{239}Pu, 16.2% ^{240}Pu, 0.41% ^{241}Pu, and 0.33% ^{242}Pu
(b)RE is composed of 0.32 at.% Ce, 0.08 at.% La, 0.20 at.% Pr, and 0.66 at.% Nd

studies on U-Pu-Am-Np-Zr alloys and oxygen-stabilized α-Zr inclusions.[5] The oxygen-stabilized α-Zr inclusions were commonly observed for U-Pu-Zr ternaries and the volume fraction of the phase varied directly with oxygen concentration, dissolving up to approximately 4 at.% uranium and 2.5 at.% plutonium.[6]

2.2 X-Ray Diffraction and Phase Identification

Three samples for phase determination were placed into a machined groove in a polycarbonate sample holder that measured 20 mm in length by 5 mm in width and 5 mm deep. The samples were placed side by side in a layer of vacuum grease that filled the machined groove. The samples were pressed into the vacuum grease using a flat surface to ensure uniform sample exposure to the x-ray beam. The samples were measured with a LaB_6 (SRM 660a) standard. The sample holder was placed in a containment chamber with a 180° beryllium window allowing for analysis of radioactive materials. XRD patterns were obtained on all three samples simultaneously employing a Scintag X1 powder diffractometer with a theta-theta goniometer configuration using Cu $K\alpha_{1,2}$ radiation at room temperature. The scan was conducted in a continuous scanning mode at 0.5° min^{-1} from 20° to 120° 2θ. The XRD data were evaluated using Rietveld analysis (Bruker AXS Topas3). XRD profiles of measured diffracted intensities were fitted using symmetrical Pseudo-Voigt (Pearson VII) profile functions.

2.3 Thermal Analysis

Transition temperatures and enthalpies of transition were determined employing a NETZSCH DSC/Thermogravimetric Analyzer (TGA) model STA 409 PC. Pt-Rh crucibles coated with yttria were used to hold the alloy sample. Ultra-high purity argon cover gas passed through an oxygen gettering furnace (OxyGon Industries, Inc. Model OG-120M) was used to conduct the experiments. Oxygen impurity levels were in the sub *ppb* range based on the measurability of the furnace. Flow rates of 50 and 20 mL min^{-1} were established for the instrument balance and sample furnace. Three consecutive DSC runs were conducted from ambient temperature to approximately 800 °C, each followed by controlled cooling to ambient temperature at a rate of 10° min^{-1}. Data was collected during both heating and cooling. Transition onset and finish temperatures were determined using NETZSCH peak deconvolution software. Enthalpies of transition were determined by integrating the full area under each transition as determined by the peak deconvolution software from transition start to transition finish.

3. Results

3.1 X-Ray Diffraction and Phase Identification

XRD patterns for the three metallic alloys investigated are provided in Fig. 2. The samples of the alloys show some

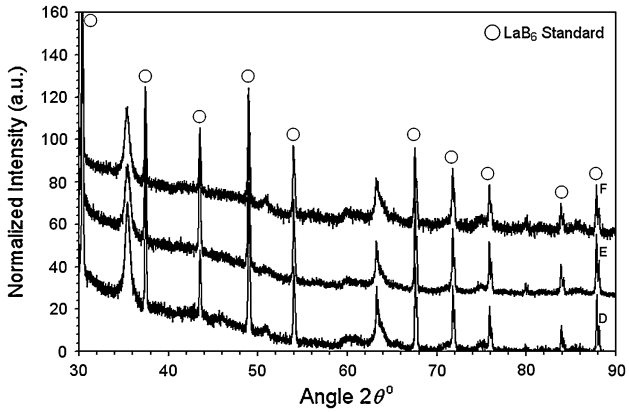

Fig. 2 X-ray diffraction patterns for the D, E, and F metallic alloys with LaB_6 (SRM 660a) standard. Alloy-D is at the bottom, and alloys progress accordingly to Alloy-F at the top

surface texture generated from the sample preparation methods, i.e., low speed sectioning of thin slices from cast fuel slugs. In addition, significant peak broadening is observed due to the nature of the samples (i.e., monolithic samples and not powder, allowing surface texture, preferred orientation effects). The Rietveld analysis accounted for these effects in both the standard and as-measured phases if needed. In order to effectively analyze the diffraction patterns with Rietveld, a sufficient knowledge of what phases are expected is necessary. Previous literature on similar U-Pu-Zr systems has suggested that there are mostly three phases present: δ-(U,Pu)Zr_2, ζ-(U,Pu), and nonequilibrium γ-U. The Rietveld analysis was conducted assuming that rapid quenching of the as-cast alloy results in a nonequilibrium microstructure, consisting of the δ-phase, ζ-phase, α-phase, and γ-phase. Relatively low refinement residuals, ranging from 6.1 to 7.0%, were obtained from the Rietveld analysis. An example of a refined Rietveld diffraction pattern for Alloy-F is provided in Fig. 3.

A summary of the quantified phase amounts is provided in Table 2, followed by the refined lattice parameter calculations for each phase and alloy in Table 3. Silcock[7] and Barnard[8] observed a hexagonal structure with a_0 = 5.03 Å and c_0 = 3.08 Å for the δ-UZr_2 phase. Calculated δ-phase lattice parameters for these alloys are slightly larger than published values (PDF pattern 34-0696). The trend is to a larger lattice parameter with increasing Zr content within the binary U-Zr system. Thus, the observed lattice parameters suggest a slightly Zr-rich δ-(U,Pu)Zr_2 phase.[9] Lawson et al. observed a rhombohedral unit cell with a_0 = 10.6853 Å and α = 89.736° for ζ-$Pu_{0.6}U_{0.4}$.[10] Calculated ζ-phase lattice parameters for these alloys are slightly larger with a slightly narrower α angle than those determined by Lawson et al. The larger lattice parameters for the alloys suggest that the U content is approximately 35 at.% or lower, meaning the alloy is Pu-rich. The remainder of the U will comprise the nonequilibrium γ-phase. Calculated lattice parameters for the γ-U phase are larger than those for published values of pure γ-U, 3.474 Å (PDF pattern 24-0749). Similar to the δ-phase, the

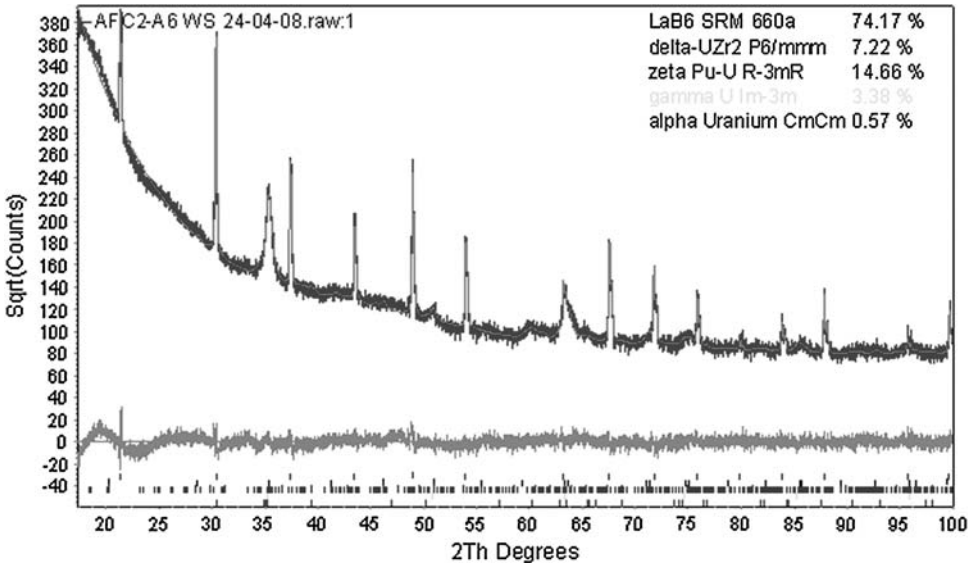

Fig. 3 Refined Rietveld diffraction pattern for Alloy-F. The peaks from 60° to 66° 2θ are characteristic of ζ-phase

Table 2 Phase contents for the D, E, and F metal alloys

Alloy	ζ-(U,Pu), %	δ-(U,Pu)Zr_2, %	α-U, %	γ-U, %	Refinement residual R_{wp}, %
D	57.2 ± 2.93	31.4 ± 0.36	0.0 ± 0.30	11.3 ± 2.30	6.05
E	56.7 ± 3.76	23.5 ± 0.47	1.4 ± 0.47	18.4 ± 2.86	7.01
F	56.8 ± 2.32	28.0 ± 2.44	2.2 ± 0.70	13.1 ± 1.20	6.29

Contents were calculated excluding the quantitative amount of the LaB_6 standard

nonequilibrium γ has dissolved a small portion of Zr, resulting in the larger lattice parameter values due to the larger atomic radius of Zr. The *bcc* γ-phase has a complete solid solubility for *bcc* ε-Pu and *bcc* β-Zr.[10] The large uncertainties associated with the calculated lattice parameters are the result of measuring sectioned samples rather than powders, translating to broadened reflections and low signal-to-noise ratios.

3.2 Thermal Properties

Heating and cooling curves obtained from the DSC measurement are provided in Fig. 4, 5, and 6 for the three alloys. Observation of the figures reveals repeatable and reproducible traces for each alloy. The first DSC run for each alloy is slightly different from the subsequent two runs, suggesting that it resulted from an annealing effect because these alloys were not heat treated prior to measurement. This is supported by the observation that the same discrepancy between the three runs does not appear upon cooling. During all of the runs for each alloy, it became apparent that two very obvious, distinct transitions are reversible upon cooling. The alloys all show a similar feature; however, the sharpness and strength of each peak varies slightly depending upon the alloy stoichiometry. A very strong or sharp peak would suggest either a single phase transition or a transition through a very narrow phase field. A broad or weak peak would suggest a transition through a wide-phase field, or an overlap of two close, consecutive phase transitions. In all cases, the cooling curves appear to resolve the more complex phase behavior than that observed upon heating.

4. Discussion

A phase diagram that represents the five major components of the alloys investigated here, excluding REs, is not available nor is it straightforward to represent these components in only two or even three dimensions. However, the five major components can be reduced to a three-component system, consisting of U-Pu-Zr, so that phase relationships can be extrapolated. Theoretically, there is minimal solubility between U and Am, especially at low temperatures, although there is very little experimental data available on this binary system.[11] Conversely, the Pu-Am binary system has been investigated experimentally and broad mutual solubility between the two has been reported.[12] For this reason, the Am content of the metal alloys is summed with the Pu content to simplify the alloy system. Np has been observed experimentally to have mutual solubility in both U and Pu,[12] so that in order to further simplify the alloy system the Np content of the metal alloys is evenly divided between the U and Pu contents. Note that the difference in atomic mass for the summing of Am with Pu, and Np with U and Pu, is not taken into account, nor is the distribution of the RE addition between the five base constituents. As this is an extremely complex

Table 3 Refined lattice parameters for the D, E, and F metal alloys

Alloy	ζ-(U,Pu), Å	δ-(U,Pu)Zr_2, Å	α-U, Å	γ-U, Å
D	$a = 10.719 \pm 0.003$	$a = 5.078 \pm 0.004$	n/a	$a = 3.592 \pm 0.003$
	$\alpha = 89.59 \pm 0.04°$	$c = 3.106 \pm 0.003$		
E	$a = 10.716 \pm 0.005$	$a = 5.092 \pm 0.007$	$a = 2.565 \pm 0.001$	$a = 3.578 \pm 0.001$
	$\alpha = 89.33 \pm 0.06°$	$c = 3.109 \pm 0.004$	$b = 5.478 \pm 0.002$	
			$c = 4.962 \pm 0.001$	
F	$a = 10.744 \pm 0.003$	$a = 5.057 \pm 0.003$	$a = 2.844 \pm 0.003$	$a = 3.596 \pm 0.001$
	$\alpha = 89.35 \pm 0.04°$	$c = 3.113 \pm 0.002$	$b = 5.861 \pm 0.006$	
			$c = 5.136 \pm 0.005$	

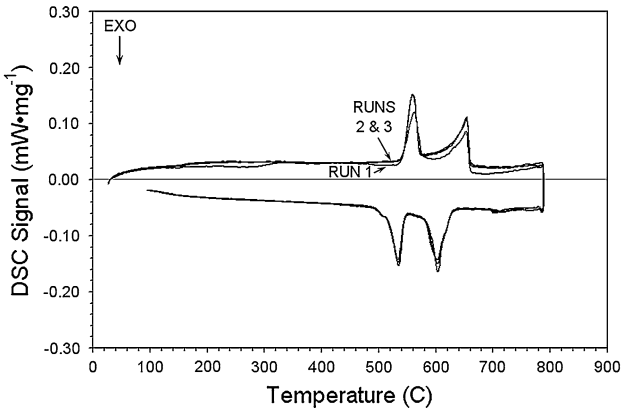

Fig. 4 Heating and cooling traces (3) obtained from the Differential Scanning Calorimeter measurements on the as-cast Alloy-D

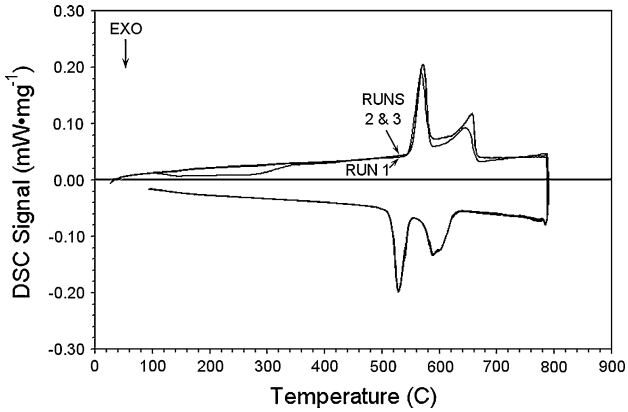

Fig. 6 Heating and cooling traces (3) obtained from the Differential Scanning Calorimeter measurements on the as-cast Alloy-F

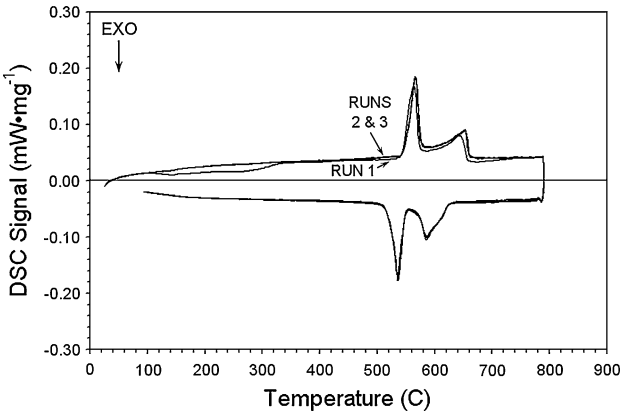

Fig. 5 Heating and cooling traces (3) obtained from the Differential Scanning Calorimeter measurements on the as-cast Alloy-E

fuel system, further experimentation on the individual binary systems, in addition to similar U-Pu-Zr alloys without Am and Pu or RE addition are needed to further confirm the proposed action and are currently underway, but not available at this time. With this in mind and for the purpose of the current study, Alloy-D (U-22Pu-4Am-2Np-40Zr-1.9RE) reduces to U-27Pu-40Zr-1.9RE; Alloy-E (U-22Pu-4Am-2Np-40Zr-1.3RE) reduces to U-27Pu-40Zr-1.3RE; and Alloy-F (U-22Pu-4Am-2Np-40Zr) reduces to U-27Pu-40Zr.

Isothermal sections of the U-Pu-Zr system are available from published literature at 773, 823, 853, 868, 913 K.[6] These diagrams will be the cornerstone for the analysis of the thermal and XRD observations, and have been reproduced in Fig. 7 indicating the position of the reduced composition for Alloy-F. The difference between the three alloys is a decrease in the U content and an increase in the RE content, so the reduced composition position is approximately in the same region for all three alloys on the ternary diagrams.

Furthermore, a room-temperature ternary phase diagram can be constructed by extrapolation from the isothermal section at 773 K and the three binary diagrams available (U-Pu, Pu-Zr, and U-Zr).[12] The ζ-phase is a complex-cubic U-Pu intermediate phase that dissolves up to 5 at.% Zr. The solubility limit of uranium in the ζ-phase is 80 at.%.[13] The δ-phase is a hexagonal U-Zr intermediate phase that occurs at approximately UZr_2 and has extensive solid solubility for plutonium. Thermodynamic calculations of the U-Pu-Zr system at 868 K performed by Kurata[14] were in good agreement with the experimental ternary diagram provided in Fig. 7, with only slight differences noted. By extrapolating the experimental ternary diagram at 773 K, considering the established boundaries represented by the binary phase

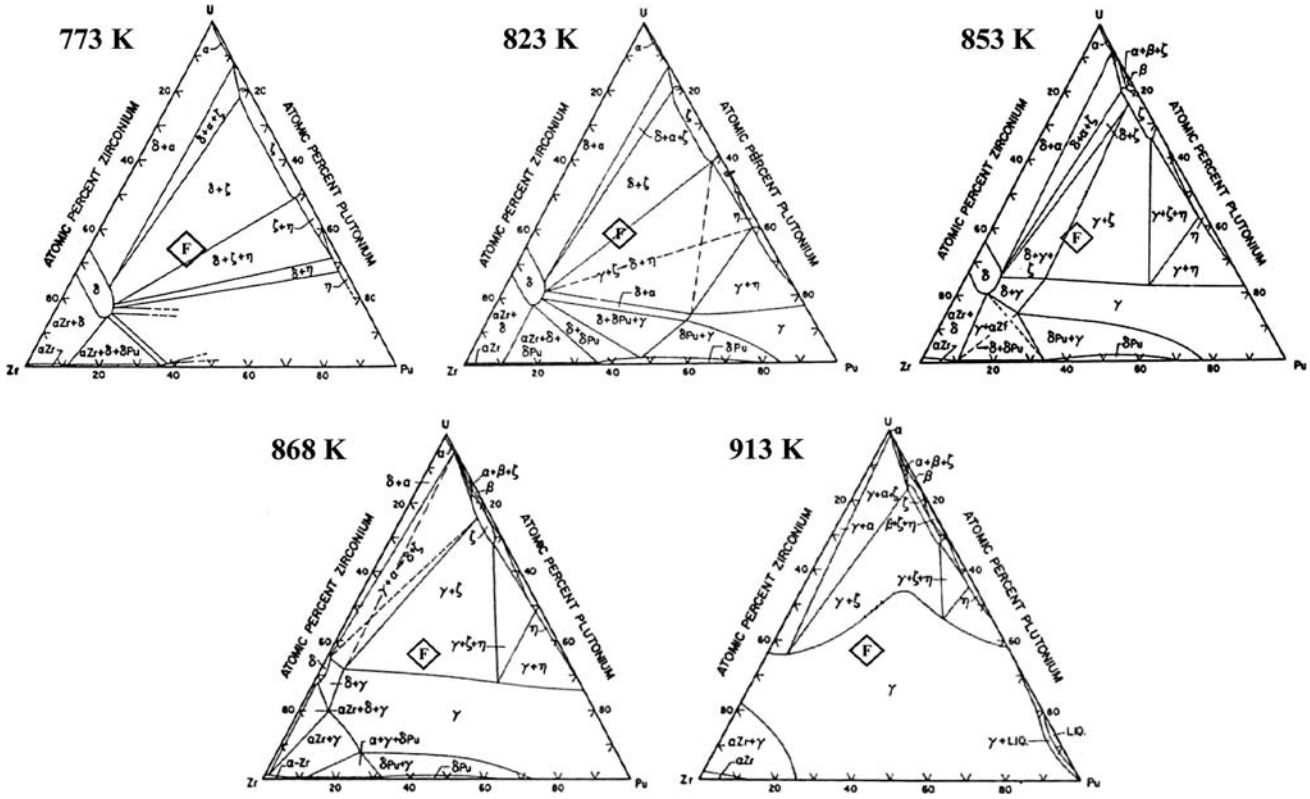

Fig. 7 Ternary U-Pu-Zr phase diagrams taken at isothermal sections of 500, 550, 580, 595, and 640 °C, after Ref 6. The reduced composition (in terms of U-Pu-Zr) for Alloy-F is marked in each diagram

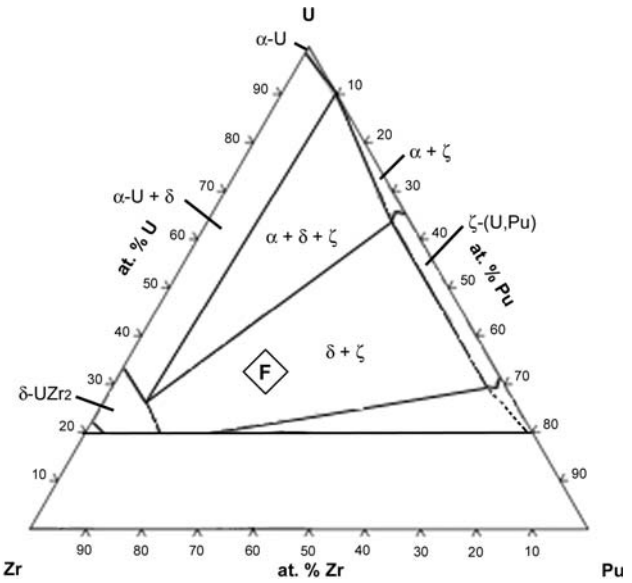

Fig. 8 A room-temperature U-Pu-Zr ternary phase diagram estimated from the five isothermal sections from Ref 6 and the three binary phase diagrams of the elements involved. The reduced composition of Alloy-F is marked on the figure

diagrams, and adhering to the rules of phase diagram construction,[15] an approximated room temperature U-Pu-Zr ternary phase diagram can be produced. The proposed room temperature ternary phase diagram is provided in Fig. 8 with the reduced composition position marked for Alloy-F. Note that since there is significant uncertainty in the Pu-Zr binary phase diagram, no attempts were made to fill in this portion of the ternary. For the current study, this seems acceptable since all of the alloys under investigation are fertile, i.e., U-rich. This diagram must be considered an approximation only, owing to the lower temperatures resulting from the extrapolated behavior. Consequently, many of the phase boundaries may not represent true behavior and further experimentation on U-Pu-Zr alloys is needed.

The room-temperature XRD measurements revealed the presence of mainly three phases: the δ-(U,Pu)Zr_2, the ζ-(U,Pu) phase, and a small amount of nonequilibrium γ-U phase for the alloys. In addition, a very minor amount of α-U phase was refined in the Alloy-E and Alloy-F XRD patterns. Observation of the extrapolated room-temperature U-Pu-Zr ternary in Fig. 7 suggests that two phases should be present in the alloy: the δ-(U,Pu)Zr_2 phase and the ζ-(U,Pu) phase. The α-U phase should not be present based on the ternary diagram. The presence of the δ + ζ phases is reasonably supported by the photomicrograph of Alloy F in Fig. 1. Approximated tie lines running through the reduced composition position suggest 59% of δ-phase, while the alloys contained approximately 26% δ-phase. A decrease in the presence of nonequilibrium γ-U phase (e.g., through post cast anneal treatment) would most likely increase the relative amount of equilibrium δ-(U,Pu)Zr_2. Most likely, the

presence of the high temperature γ-phase results from a nonequilibrium microstructure upon rapid quenching of the cast alloys. Furthermore, since all three alloys contained oxygen-stabilized α-Zr, although not enough to be detected by XRD, the amount of δ-(U,Pu)Zr_2 phase would be expected to be lower than predicted.

Observation of the reduced alloy composition in Fig. 7 and 8 shows that there should be three distinct transitions: (i) $\zeta + \delta \rightarrow \delta + \zeta + \gamma$; (ii) $\delta + \zeta + \gamma \rightarrow \zeta + \gamma$; and (iii) $\zeta + \gamma \rightarrow \gamma$. Observation of the heating and cooling traces in Fig. 4 through 6 does not reveal three distinct endotherms (heating) and exotherms (cooling). Rather, two large and convoluted transitions can be observed upon heating and cooling, although upon cooling an additional transition is much more apparent. Transition temperatures and enthalpies can be determined by deconvolution of the traces armed with the knowledge of three-phase transitions and the expected location where such transitions can occur. The first transition ($\delta + \zeta \rightarrow \delta + \zeta + \gamma$) should occur between 823 and 853 K. The second transition ($\delta + \zeta + \gamma \rightarrow \zeta + \gamma$) should occur between 853 and 868 K. Finally, transition of $\zeta + \gamma \rightarrow \gamma$ should occur below 913 K. Initial guesses for the onset of phase transitions were selected based on these transition temperature ranges. The peaks were fit to a Fraser-Suzuki profile that allows a variable amount of asymmetry in the curve.[16] The values obtained by deconvolution of the DSC traces are summarized in Table 4 for each of the alloys upon heating and in Table 5 upon cooling. An example of the deconvoluted DSC trace for Alloy-F upon heating and cooling is shown in Fig. 9.

The $\delta + \zeta \rightarrow \delta + \gamma + \zeta$ transition temperatures range from 816 to 826 K upon heating and 818 to 820 K upon cooling, very close to the predicted transition temperature range of 823 to 853 K. The enthalpies associated with this transition are reversible upon heating and cooling of the alloys. The alloys should be composed of approximately 44% ζ-phase and 56% δ-phase at 773 K. Based on the room temperature XRD measurements, this means that a portion of the ζ-phase has transformed to δ-phase upon heating from room temperature, which contained ~57% ζ-phase. The transition temperature decreased slightly with increased RE amounts, suggesting that the addition of REs to the alloy will shift the composition toward the Zr-Pu portion of the ternary phase diagram from Alloy-F in Fig. 7. Furthermore, the enthalpy associated with this transition also decreased with the addition of REs to the alloy. Above 823 K, the $\delta + \zeta$ phase has transitioned into the narrower $\delta + \gamma + \zeta$ three-phase field. Rietveld analysis on the room temperature XRD measurements revealed that the alloys had consistent amounts of ζ-phase, approximately 57%, while Alloys-E and -F had lower amounts of δ-phase, approximately 25%, and higher amounts of γ-phase, approximately 15%. In addition, Alloys-E and -F also had small amounts of α-U phase. The alloys should contain mostly δ-phase at this temperature, compared to $\zeta + \gamma$ phases. Thus, because Alloy-D has the most δ-phase and no presence of α-U phase, this alloy should have the lowest enthalpy of transition. Similarly, while Alloys-E and -F have lower amounts of δ and higher amounts of α-U, more conversion to δ-phase is necessary, resulting in higher enthalpy of transition values. It follows that Alloy-F has the most amount of α-U phase and thus will have a higher enthalpy of transition than Alloy-E.

Table 4 Transition temperatures (T_{tr}) and enthalpies of transition (ΔH_{tr}) determined from differential scanning calorimetry upon heating of the alloys

Alloy-D			
Transition	$\delta + \zeta \rightarrow \delta + \zeta + \gamma$	$\delta + \zeta + \gamma \rightarrow \zeta + \gamma$	$\zeta + \gamma \rightarrow \gamma$
T_{tr}, K	816 ± 1.4	875 ± 3.6	913 ± 1.1
ΔH_{tr}, J g^{-1}	11.3 ± 0.07	7.4 ± 1.27	5.1 ± 0.56
Alloy-E			
Transition	$\delta + \zeta \rightarrow \delta + \zeta + \gamma$	$\delta + \zeta + \gamma \rightarrow \zeta + \gamma$	$\zeta + \gamma \rightarrow \gamma$
T_{tr}, K	822 ± 2.8	870 ± 4.7	900 ± 9.7
ΔH_{tr}, J g^{-1}	12.4 ± 0.47	3.0 ± 1.16	5.2 ± 0.99
Alloy-F			
Transition	$\delta + \zeta \rightarrow \delta + \zeta + \gamma$	$\delta + \zeta + \gamma \rightarrow \zeta + \gamma$	$\zeta + \gamma \rightarrow \gamma$
T_{tr}, K	826 ± 2.6	879 ± 7.2	912 ± 12.5
ΔH_{tr}, J g^{-1}	15.3 ± 1.08	7.5 ± 1.98	4.2 ± 1.67

Table 5 Transition temperatures (T_{tr}) and enthalpies of transition (ΔH_{tr}) determined from differential scanning calorimetry upon cooling of the alloys

Alloy-D			
Transition	$\delta + \zeta + \gamma \rightarrow \delta + \zeta$	$\zeta + \gamma \rightarrow \delta + \zeta + \gamma$	$\gamma \rightarrow \zeta + \gamma$
T_{tr}, K	818 ± 0.1	886 ± 2.4	901 ± 1.4
ΔH_{tr}, J g^{-1}	−10.7 ± 0.12	−7.2 ± 1.14	−8.2 ± 1.03
Alloy-E			
Transition	$\delta + \zeta + \gamma \rightarrow \delta + \zeta$	$\zeta + \gamma \rightarrow \delta + \zeta + \gamma$	$\gamma \rightarrow \zeta + \gamma$
T_{tr}, K	820 ± 0.1	872 ± 0.2	897 ± 0.4
ΔH_{tr}, J g^{-1}	−12.6 ± 0.04	−3.4 ± 0.22	−6.9 ± 0.19
Alloy-F			
Transition	$\delta + \zeta + \gamma \rightarrow \delta + \zeta$	$\zeta + \gamma \rightarrow \delta + \zeta + \gamma$	$\gamma \rightarrow \zeta + \gamma$
T_{tr}, K	819 ± 0.6	877 ± 1.2	896 ± 0.2
ΔH_{tr}, J g^{-1}	−16.0 ± 0.14	−8.9 ± 0.34	−5.9 ± 0.29

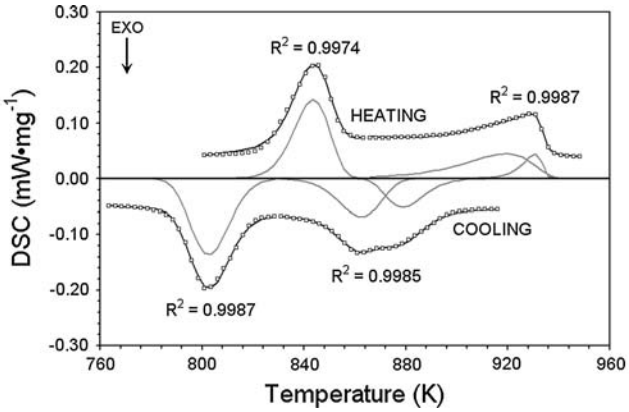

Fig. 9 Deconvoluted DSC trace for Alloy-F. The anticipated transitions (3) could be reasonably separated from the experimental data with correlation coefficients listed on the figure

At 868 K, the $\delta + \gamma + \zeta$ phase should have transitioned into the $\gamma + \zeta$ two-phase field based on the ternary phase diagram predictions. A tie line drawn through the position of the reduced composition suggests approximately 52% γ and 48% ζ. The onset temperatures for this transition obtained during heating ranged from 870 to 879 K and from 872 to 886 K during cooling, with the transition temperature remaining fairly constant for each alloy. These ranges are slightly above the predicted transition in the range of 853 to 868 K. In addition, no clear dependence upon the enthalpy is associated with this transition on alloy composition. Alloy-E had the lowest enthalpy of transition, while Alloys-D and -F had comparable enthalpies of transition. The lower enthalpy of transition into the $\delta + \gamma$ phase for Alloy-E results from the higher nonequilibrium γ-phase content of this alloy ($\sim$18.4%) measured by XRD at room temperature. Alloys-D and -F had comparable amounts of nonequilibrium γ-phase ($\sim$11 to 13%), meaning that more of the ζ-phase must convert to γ-phase resulting in higher enthalpy of transition values than those observed for Alloy-E.

The $\zeta + \gamma \rightarrow \gamma$ transition temperatures range from 900 to 913 K upon heating and from 896 to 901 K upon cooling, well below the maximum transition temperature of 913 K. The enthalpies associated with this transition do not show any clear trend as a function of alloy composition and are within the standard errors of one another upon heating. Upon cooling, the phase transition temperature similarly does not show a clear trend as a function of alloy composition, while the enthalpy associated with the transition clearly has higher values than those obtained during heating and typically increase in value with increased RE content. The reason behind these discrepancies is not well understood at this time. Decreasing the heating rate and/or employing helium rather than argon might help resolution of this peak and will be investigated at a later date in more detail. On a final note, it appears that all values obtained from the cooling traces are more reliable and consistent than those obtained from the heating traces.

5. Conclusions

Metallic fuel alloys are under consideration for the transmutation of MAs in fast reactors. As part of the reprocessing scheme, a small percentage of RE elements are carried over for recycle of spent nuclear fuel. Thermal and phase behavior of a U-22Pu-4Am-2Np-40Zr base alloy along with additions of 1.3 to 1.9 at.% RE consisting of lanthanum, cerium, praseodymium, and neodymium were investigated and discussed. The addition of RE metals to the U-Pu-Zr-Am-Np alloy did not have an influence on the room-temperature phases present, although a significant amount of nonequilibrium γ-U phase ($>11\%$) was observed in the as-cast alloys. Phase transition temperatures were relatively independent of the alloy composition and RE content, while the enthalpies of transition appeared to heavily depend on the phases present in the as-cast alloy, mainly through the increased presence of nonequilibrium γ-U phase at room temperature. Through deconvolution of the thermal analysis traces, reasonable transition temperatures and enthalpies were obtained; however, in the future a slower heating rate and use of a higher thermal conductivity cover gas should be employed. The transitions associated with the alloys compare very well with those predicted by U-Pu-Zr ternary diagrams.

Acknowledgments

This work is supported by the U.S. Department of Energy, Office of Nuclear Energy (NE), under DOE Idaho Operations Office Contract DE-AC07-05ID14517. The authors are especially grateful to the INL Analytical Laboratory (AL) and Fuel Manufacturing Facility (FMF) staff. The authors wish to specifically acknowledge Mr. Andrew Maddison, Dr. Steven Frank, Mr. Timothy Hyde, Mr. Jim Stuart, Mrs. Cynthia Papesch, Mr. Jim Morrison, Mr. Scott Wilde, Mr. Benjamin Krause, and Dr. Marsha Lambregts for their assistance with fabrication, sample preparation, and material transfers related to these experiments. Finally, the authors would like to acknowledge the Health and Physics staff for their continued support of this work in the AL and FMF facilities.

U.S. Department of Energy Disclaimer

References

1. L. Burris, R.K. Steunenberg, and W.E. Miller, "The Application of Electrorefining for Recovery and Purification of Fuel Discharged from the Integral Fast Reactor," AICHE Symp. Series No. 254 83, 1987, p 135
2. Y.I. Chang, The Integral Fast Reactor, *Nucl. Tech.*, 1989, **88**, p 129
3. D.E. Burkes, R.S. Fielding, D.L. Porter, D.C. Crawford, and M.K. Meyer, A U.S. Perspective on Fast Reactor Fuel Fabrication Technology and Experience, Part I: Metal Fuels and Assembly Design, *J. Nucl. Mater.*, 2009, **389**, p 458-469
4. T. Hyde, "Fabrication Report for the AFC-2A and AFC-2B Capsule Irradiations in the ATR," INL/EXT-13021, Idaho National Laboratory, 2007
5. J.R. Kennedy and D. Janney, "The Phase and Microstructure Characterization of AFC 2A Metallic Transmutation Fuels: FY

2007 Report," Idaho National Laboratory, INL/EXT 13027, 2007
6. D.R. O'Boyle and A.E. Dwight, *Proceedings of the 4th International Conference on Pu and Other Actinides*, Santa Fe, NM, 1970, Session 2, p 720
7. J. Silcock, Intermediate Phase in the Uranium-Zirconium System, *Trans. AIME*, 1957, **209**, p 521
8. R.D. Barnard, Electrical and Magnetic Properties of Uranium-Niobium System, *Proc. Phys. Soc. London*, 1961, **78**, p 363-369
9. M. Akabori, A. Itoh, T. Ogawa, F.. Kobayashi, and Y. Suzuki, Stability and Structure of the δ Phase of the U-Zr Alloys, *J. Nucl. Mater.*, 1992, **188**, p 249
10. A.C. Lawson, J.A. Goldstone, B. Cort, R.J. Martinez, F.A. Vigil, T.G. Zocco, J.W. Richardson, Jr., and M.H. Mueller, Structure of ζ-phase Plutonium-Uranium, *Acta Cryst.*, 1996, **B52**, p 32-37
11. T. Ogawa, Alloying Behaviour Among U, Np, Pu and Am Predicted with the Brewer Valence Bond Model, *J. Alloys Comp.*, 1993, **194**, p 1
12. T.B. Massalski, Ed., *Binary Alloy Phase Diagrams*, 2nd ed., Vol. 3, ASM International, 1990
13. G.R. Grove, "Reactor Fuels and Materials Development, Plutonium Research: 1966 Annual Report," USAEC Report MLM-1402, 1967
14. M. Kurata, Thermodynamic Assessment of the Pu-U, Pu-Zr, and Pu-U-Zr Systems, *Calphad*, 1999, **23**, p 305-317
15. F.N. Rhines, *Phase Diagrams in Metallurgy, Metallurgy and Metallurgical Engineering Series*, McGraw-Hill, New York, 1956
16. R.D. Fraser and E. Suzuki, Resolution of Overlapping Bands. Functions for Simulating Band Shapes, *Anal. Chem.*, 1969, **41**, p 37